Forces in Mechanics 4 (2021) 100033

Contents lists available at ScienceDirect

Forces in Mechanics

journal homepage: www.sciencedirect.com/journal/forces-in-mechanics

Grain boundary engineering of new additive manufactured polycrystalline alloys

Frank Abdi [a,e], Amirhossein Eftekharian [a], Dade Huang [a], Raul B. Rebak [b], Mohamed Rahmane [b], Veera Sundararaghavan [c], Alec Kanyuck [d], Satyandra K. Gupta [d], Senthil Arul [f], Vaibhav Jain [f], Yun Hu [e], Kamran Nikbin [e]

[a] AlphaSTAR Corporation, Irvine, CA, United States
[b] General Electric Global Research Center (GERC), Albany, NY, United States
[c] University of Michigan, Ann Arbor, MI, United States
[d] University of Southern California, Los Angeles, CA, United States
[e] Imperial College London, South Kensington Campus, United Kingdom
[f] Defense Logistic Agency, Fort Belvoir, VA, United States

ARTICLE INFO

Keywords:
Additive Manufacturing
Grain Boundary Engineering
Meltpool Engineering
Mechanical/Fracture/Fatigue Properties
Low/High Grain Boundary Microstructure
Thermal Management

ABSTRACT

A novel idea to create new alloys for Additive manufacturing (**AM**) by mixing a small addition of nanoparticles with bulk material was put forward. Integrated Computational Material Engineering (**ICME**) may be used to guide the AM process, predict thermal behaviour, optimize process parameters, secure net-shape, and qualify parts. Modelling is needed to predict the effect of defects and the effect of inclusions on mechanical properties, build quality and in-service performance. ICME can reduce *trial-and-error* fabrication and establish an AM digital twin, thereby accelerating part qualification and AM adoption. AM creates complex thermal processes which impact material microstructure and result in changes to mechanical properties in terms of strength and plasticity. In this study, Grain-Boundary Engineering (**GBE**) and multi-scale modelling are performed to expedite qualification of new and existing AM polycrystalline alloys.

AM parts exhibit cracks, low toughness, low plasticity, and high residual stresses. To mitigate these characteristics, a methodology for GBE and microstructural control was developed. Depending on part requirements a low angle, coincident site lattice, or high angle grain boundary (**LAGB,CSL, HAGB**) might be the preferred option. For example, HAGB occurs in equiaxed grain microstructure, prevents precipitation and crystallization formation, and inhibits cracks and corrosion. Some polycrystalline materials may be non-weldable and exhibit cracks. Microstructural control can be used to address this phenomenon. AM offers unique advantages over casting, including material composition change and unique thermal processing. By utilizing nano-inclusions, cracks may be mitigated and AM parts improved.

ICME physics-based approach is used to implement GBE modelling to improve the microstructure of an AM polycrystalline material from Equiaxed/HAGB to LAGB and CSL considering nano-scale inclusions. The ICME tool integrates meltpool engineering; thermal transport; nano-micro-mechanics; material characterization; calibration and qualification; Voronoi-tessellation, finite element modelling, and design of experiment optimization. With this background, ICME predicts time-temperature transformation, thermal properties, process map, meltpool size, precipitation, porosity, and effects of nano inclusions. In this manner, ICME helps determine ideal AM machine parameters that secure qualified parts as a consequence of the AM process.

In this study, mechanical properties and fracture toughness were validated against test. Predictions included creep, crack growth, and the effect of precipitates and voids under in-service crack growth behaviour. Stainless steel (SS316L) dog bones specimens were printed and stress relieved by air and water cooling supported by fractography and imaging. The objective of this effort was to develop technologies and processes in AM design and engineering that could predetermine the microstructure of AM parts. Future efforts will employ the tool to tailor grain boundaries to produce predictable mechanical properties - including mode of failure.

E-mail address: fabdi@alphastarcorp.com (F. Abdi).

https://doi.org/10.1016/j.finmec.2021.100033
Received 16 March 2021; Received in revised form 29 May 2021; Accepted 7 July 2021
Available online 21 July 2021

Nomenclature

AM	Additive Manufacturing
ASC	AlphaSTAR Corporation
CSL	Coincident Site Lattice
DOE	Design of Experiments
D&DT	Durability and Damage Tolerance
GB	Grain Boundary
GBE	Grain Boundary Engineering
GMDC	Grain Modelling Diffusional Creep
EBSD	Electron Backscatter Diffraction
ECAP	Equal-Channel Angular Pressing
FEM	Finite element model
FCG	Fatigue Crack Growth
FSW	Friction Steer Welding
FTD	Fracture Toughness Determination
HIP	Hot Isostatic Pressing
ICME	Integrated Computational Material Engineering
IHT	Intrinsic Heat Treatment
LAGB	Lower Angle Grain Boundary
HAGB	High Angle Grain Boundary
KAM	Kernel Average Misorientation
MPE	Melt Pool Engineering
MRF	Markov Random Field
NAM	Nano-Assisted Micro-mechanics
RGB	Red–green–blue colour space
PHT	Post Heat Treatment
PMO	Process Model Optimization
SA	Solution Annealing
SAED	Selected Area Electron Diffraction
SCC	Stress Corrosion Crack
SEM	Scanning Electron Microscopy
SR	Stress Relieved
TTT	Temperature Time Transformation
TTP	Temperature Time Precipitate
TMg	Thermal Management
ZOM	Zeroth-Order Model

1. Introduction

The quest to accelerate and shorten the current 20-year time consuming material development of new polycrystalline alloys stems from the DARPA Accelerated Material Initiative and the White House Office of Scientific Research GENOM program. The recent success to open variety of ways for producing ultrahigh strength material was achieved by Ashby's [1] Damascus steel template, which suggests that high powered lasers may be used as tools for the hardening of steels. When the energy, diameter, and speed of the beam are adjusted to transform the surface to austenite, self-quenching by conduction into the cold metal beneath the surface transforms the austenite to martensite. The technique gives a hard, wear-resistant surface with less distortion than that caused by flame or induction hardening, and it lends itself to precise numerical control and automation. Studies of this transformation hardening show that results depend on ***process variables:*** power, size, and shape of the laser beam, scan velocity, chemistry and metallurgy of steel, and Langdon [2] ultra-fine equiaxed grains to change material microstructure and improve strain and strength performance. For example [4] GE's successful patent made it possible to design the grain size and grain boundaries of the net-shaped parts by altering the process parameters to minimize surface roughness during the AM process. The benefits of AM to achieve multifunctional material, considering nanocomposite [3] inclusions, exothermic effect (heat generation), and ultra-fine grain formation techniques may be achieved by adding nano/micro particles, and considering the defects (i.e., void, surface roughness) and failure mechanisms associated with AM, which may be best served by ICME technology .

Grain Boundary Engineering is a critical science to improve quality and reliability of AM parts. Design for improved steel performance by **1**) alloy modification with inclusion effects on microstructure, **2**) grain crystallization to achieve CSL grain boundaries and LAGB formations by alternating intrinsic heat treatment (**IHT**), and/or acoustic meltpool excitation during AM Process, and **3**) post-heat treatment to improve steel mechanical properties including elongation (i.e. plasticity), yield, and ultimate strength and fracture property performance. The Objective is to develop technologies and processes in AM design and engineering procedures that can predetermine the microstructure of AM parts with "tailored" grain boundaries to produce predictable mechanical properties - including mode of failure.

ICME exploration of GBE during AM or post build processes includes thermal heating, fast cooling, inclusions, and meltpool excitation to predict the formation of CSL and LAGB grain boundaries. This includes an assessment of inclusion effects on microstructure and material performance, such as induced plasticity. For example, Tungsten debris during friction steer welding (**FSW**) of titanium has been shown to produce cracks and damage in a built part. Here, ICME simulates inclusions and precipitates to obtain sub-grain crystallization and performs optimization of machine parameters (i.e., power, speed, hatch space, layer thicknesses), to minimize defects (voids, surface roughness, and residual stress) and track damage. Integration of the ICME tool set with 3D EBSD visualization *for the Design of GBE to predetermine* the microstructure of AM parts (Figure 1) includes: **1**) micro-thermal management (**TMg**): prediction of thermal and material states, phase diagram and crystallization, and process map; **2**) grain modelling diffusional creep (**GMDC**): prediction of intergranular, transgranular cracks, surface roughness, and residual stress; **3**) process model optimization (**PMO**): optimized CSL/LAGB formation and 3D ESBD

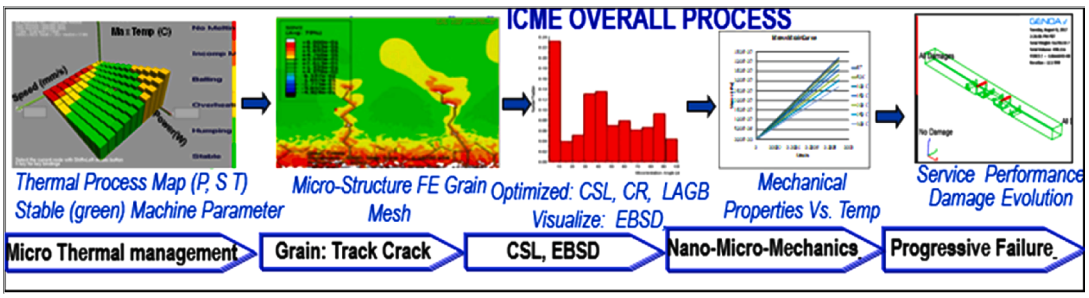

Figure 1. ICME Design of Grain Boundary Engineering (GBE)

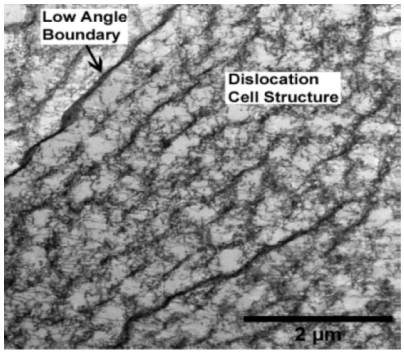

Figure 2. GE TEM image of sub-grain dislocation cellular structure and boundary structure in AM SS-316L after stress relief [4]

visualization; **4**) nano-assisted micro-mechanics (**NAM**): analytical model to determine mechanical (strength, stiffness) and fracture and fatigue properties versus temperature considering defects; and **5**) service model: performance and prediction of tensile strength, and stress-strain curve (yield, ultimate, plasticity), and scatter in mechanical properties.

1.1. Background

AM parts produced by machine modalities such as laser powder bed fusion (**LPBF**) (i.e. Concept Laser, EOS), or electron beam (i.e. ARCAM) may exhibit lower plasticity/strain in comparison to traditional/conventional manufacturing (i.e. casting, forming and forging). AM parts therefore are subject to crack formation, oxidation, and creep corrosion in service environment. Post heat treatment (**PHT**) reduces residual stress in these parts, but may also cause grain-growth, loss of plasticity, and damage. A non-grain growth morphology is needed; some authors have suggested inclusions may address the undesired phenomena. An ideal alloy should be strengthened by hard dispersed second-phase particles. The particles should be as fine as possible, but greater than the bypass size of about 1 nm, to minimize crack nucleation or decohesion. The volume fraction should be as large as possible without exceeding the percolation limit at which particle-particle contact becomes highly probable. Precipitation hardening, solid solution hardening, grain size minimization, and deformation each may promote secondary hardening. The cohesive strength of the particle interface should be high. Impurities and large inclusions should be avoided. Many of these requirements have been demonstrated in rapid solidification technology alloys.

In such alloys segregation is minimized, and the averaging of particles formed during solidification and cooling is suppressed. Thus, the fine dispersoids desirable for strength can be formed. Figure 2 shows GBE after AM part post-heat treatment (stress relief heat treatment) of stainless steel, which accomplished the formation of CSL and LAGB grain boundaries. Dislocation entanglement creates dislocation cells inside the grain. Cell walls are formed by dislocation tangling and are oriented parallel to the thermal gradient from laser solidification. LAGB are also formed by highly concentrated dislocation clusters. The sub-grain dislocation structure is like cold worked stainless steel and oriented primarily towards the build direction.

The AM industry would like to know how GBE can become more efficient in AM preferably during AM process, not after AM post heat treatment. Similarly, good progress on GBE was achieved in friction stir welding [5] on polycrystalline material where crystallization, equiaxed sub-grain, LAGB, formation was formed up to 10 degrees misorientation angle using a faster cooling approach with/without inclusion effect.

Inclusion Effect - In AM, it would be possible to design the grain size and grain boundaries of the net-shaped parts by altering the print path and by adding nano/micro particles in a specific localized region during the AM process. Figure 3 shows the ICME based approach and the resulting new alloy composition and design. This includes: **1**) effect of Powder composition and distribution on microstructure; **2**) inclusion effect on polycrystalline metal and improvement of material mechanical properties and performance, namely ductility fracture and fatigue properties.

These ingredients have effect on strength, hardness, ductility and toughness, fatigue, formability, machinability, weldability, and corrosion. These ingredients can be one or a mixture of the following**:** carbon, silicon, manganese, chromium, molybdenum, nickel, aluminium, niobium, titanium, vanadium copper, boron, nitrogen, tungsten, cobalt. Key impurity compositions offer improvement in: **a**) ductility and toughness by phosphorus, and sulfur; **b**) durability by chromium; **c**) bonding and diffusion by nickel together develop a new multi-functional polycrystalline alloy material. EBSD can be used to determine crystallographic orientation and phase identification in polycrystalline materials (i.e., steel, titanium, aluminium etc.). In addition to assist GBE, ICME incorporates precipitate formation by considering the phase, TTT, and TTP diagrams.

1.2. Literature Overview

1.2.1. Inclusion effect on Microstructure Transformation and Material Strength

The strengthening and weakening of the textures can be understood in part by comparison to ideal shearing textures and by analysis of the flow in terms of level of spin superimposed on shearing deformations. This suggests that the strength of material is determined both by LAGB and HAGB. Moreover, nanocomposites deformed at high temperature and high strain rate. It is reported that transformation of LAGB into HAGB effectively takes place when the boundaries are pinned by small particles that form at faster rates in the presence of bimodal sized particles. With an increase in temperature there is a decrease in low-angle misorientation and an increase in high-angle misorientation. Here, it should be noted, LAGB's are responsible for the formation of dislocation substructures and subsequently sub-grains **[**6**]**.

1.2.2. Electron Backscatter Diffraction (EBSD)

was first observed by Kikuchi in 1928 through scattering of the incident beam within a specimen. Use of this technique expanded to scanning electron microscopy by applying Kossel x-ray diffraction to determine the diffraction pattern centre and to measuring lattice parameters from the Kikuchi lines. Automated EBSD and the development of orientation imaging microscopy led to widespread use in determining crystallographic orientation and phase identification in polycrystalline materials. A new numerical method is presented for reconstructing 3D

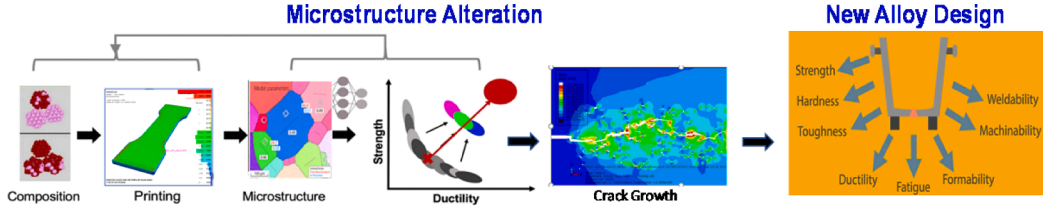

Figure 3. Schematic highlight of ICME based new alloy design

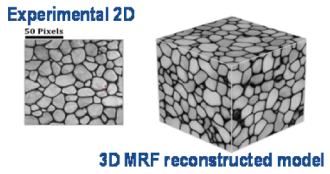

Figure 4. Innovation 3.1-Polycrystalline 3D ESBD visualization grain recognition [7]

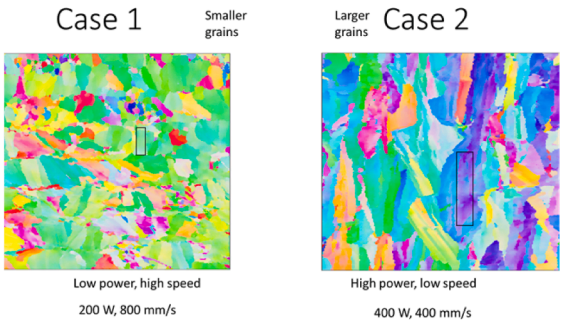

Figure 5. Stainless steel 316-3D EBSD visualization grain recognition

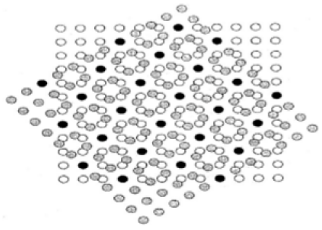

Figure 6. Two overlaying lattices (grey, white), with black atoms being CSL & 5 relationship [8]

microstructures from 2D sections, imaged on orthogonal planes, by exploiting the complete red–green–blue (**RGB**) colour space. The algorithm reconstructs 3D models through sampling voxel neighbourhoods to represent 2D micrographs, based upon a Markovian assumption. The sampling is followed by an optimization procedure which ensures smoothness across the orthogonal sections of the synthesized voxels. Previous 3D Markov random field (**MRF**) microstructure reconstruction techniques were restricted to traditional grayscale images only. This method now enables the use of the entire RGB spectrum, which also employs a histogram matching step. This method examines the algorithm's accurate representation of orientations and morphologies, encompassing a variety of micrographs from EBSD and polarized light microscopy. The 3D reconstruction is shown in Figure 4. Figure 5 shows stainless steel 316- 3D EBSD visualization grain recognition. The EBSD grain recognition and reconstruction used LPBF process: a) Case 1: low power (200 W), and high speed (800mm/s), and b) Case 2: high power (400 W) and low speed (400mm/s). resulting in smaller and larger grain microstructure.

1.2.3. CSL boundaries

Kronberg and Wilson were the first to introduce the concept and importance of the coincident site lattice theory (CSL) theory [8]. CSL's are defined by the finite fraction of crystal lattice sites that coincide between the two lattices. The quantity sigma (**Σ**) is then defined as the volume ratio between the unit cell of coinciding sites and a standard unit cell, which is also the reciprocal density of coinciding sites. An example of a (**Σ5**) relationship is shown in Figure 6. It should be noted that the CSL theory is only a geometrical concept, and as such, any boundary can

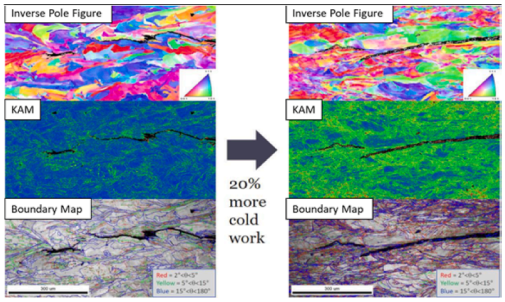

Figure 7. General Electric EBSD mapping of a stress corrosion crack in the stress-relieved AM 316L SS tested in the X-Z orientation [9]

be defined as a CSL boundary provided that the sigma value is allowed to approach infinity.

1.2.4. Equiaxed Ultrafine Grain

A technique, proposed by Langdon [2] that describes ultrafine grains in metals and alloys and underlies a very significant enhancement in their mechanical and functional properties to achieve advanced properties after processing by equal-channel angular pressing (**ECAP**). It is necessary to control a wide range of microstructural parameters including the grain boundary misorientations, the crystallographic texture, and the distributions of any second phases.

During the last decade, ECAP has emerged as a widely known procedure for the fabrication of ultrafine-grained metals and alloys for grain refinement. This includes modifying conventional ECAP to increase the process efficiency and techniques for up-scaling the procedure and processing of hard-to-deform materials. Special attention is given to the basic principles of ECAP processing including the strain imposed in ECAP, the slip systems and shearing patterns associated with ECAP, and the major experimental factors that influence. Attention is directed to the significant features of the microstructures produced by ECAP in single crystals and polycrystalline materials with both a single phase and multi-phases.

Low angle grain: The results from these experiments revealed two important trends. First, there was an increase in the equilibrium grain size with increasing temperature. Second, it was concluded from an examination of the selected area electron diffraction (**SAED**) patterns that the fraction of low-angle grain boundaries increased with increasing temperature due, it was suggested, to the faster rates of recovery at the higher temperatures which led to an increasing annihilation of dislocations within the grains and a consequent decrease in the numbers of dislocations absorbed into the sub-grain walls. Low-angle grain boundaries increased with increasing temperature due, it was suggested, to the faster rates of recovery at the higher temperatures which led to an increasing annihilation of dislocations within the grains and a consequent decrease in the numbers of dislocations absorbed into the sub-grain walls.

1.2.5. Stress Corrosion Crack (SCC)

For AM 316L SS, the cracking of the stress-relieved material showed a mixed contribution from low and high angle boundaries of columnar structures and dendrites, with some intragranular morphology. The presence of sub-grain deformation structures and the distribution of cold work associated to these structures served as the driving force for SCC. Figure 7 (left) shows the EBSD map of the crack front (X-Z orientation) in the non cold worked AM 316L SS. The inverse pole figure (crystallographic texture map) and boundary map show that part of the crack followed the high angle boundary between two grains. Although the boundaries were tortuous in the material, the boundaries of the elongated grains in the material build direction formed an easier crack path. The high angle boundaries were not the only path for SCC. The left and right portions of the crack did not follow high angle boundaries. Instead,

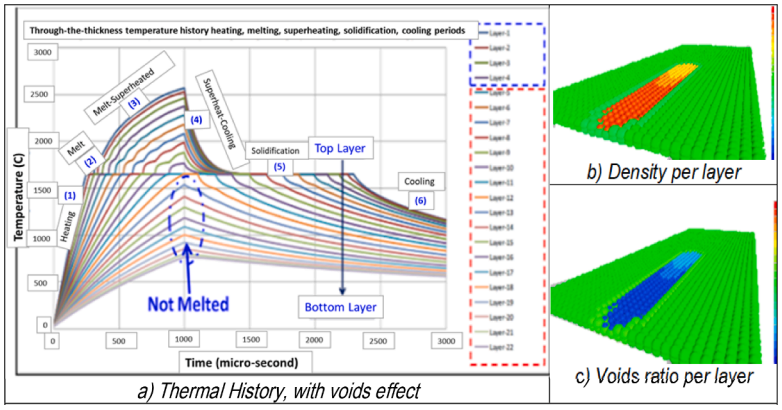

Figure 8. Ti64 Microscale Thermal Management History

the crack followed sub-grain structures, which could be the low angle columnar boundaries or dislocation cells. Kernel average misorientation (**KAM**) maps provide direct evidence of localized orientation changes such as dislocation cells, columnar structures, and sub-boundaries, all of which are associated with the strain distribution.

These sub-grain deformation structures were also distributed in the material build direction. The alignment of these structures and the strain distribution served as the main driving force for the crack to follow the build direction. Figure 7 (right) shows that after 20% cold work was applied to the material, the sub-grain deformation structures were enhanced and further connected along the material build direction. The grains were deformed in the forging plane. The crack was straight without a tendency to follow any preferred pre-existing boundaries. Corrosion products were observed inside the crack.

2. Methodology and technical approach

The technical approach includes the following steps: **1**) adopt GE patent on stainless steel; **2**) perform GBE with inclusion in Polycrystalline Steel; **3**) optimize the Thermal management to obtain temperature profile, micro voids, and crystallization; **4**) obtain CSL-LAG, with maximum residual strain in some of the powders; **5**) perform GBE by heating and reheating, melt excitation, fast cooling, minimize grain growth, and cracks; **6**) extend mechanical strength and fatigue properties; **7**) design GBE by ICME methods.; **8**) validate by printing coupons using commercial machine; **9**) perform post heat treated of coupons with NDE measurements.

In pursuit of GBE, the team implemented a comprehensive ICME methodology that drove the AM build to improve material reliability with optimized plasticity, activate sub-grain formation and recrystallization, reduce AM defects and surface roughness, predict service load under static loads of AM metallic parts, and control the manifestation of residual strain as needed for GBE. The referenced alternative methods are applied individually and in collaboration with each other. As noted, ICME supported sensitivity analysis and Design of Experiment (DOE) work to identify an ideal combination, if it exists. It is assumed that laser heating and reheating, supported by melt pool excitation by sound wave and fast cooling with Argon, achieve desired crystallization with equiaxed grains. The use of inclusions (mixed powders, such as Mg, Si) are evaluated to generate the desired GBE outcome or trigger the formation of precipitates that ultimately support that effort. The formation of fine grain, CSL, and LAGB result in better plasticity and higher resistance to oxidation and corrosion within the finished article.

2.1. Thermal Management (TMg) – Micro-Macro -Thermal Transport

Predict/Validate: (i) Process Map, (ii) Thermal State (Figure 8a: heating, Melting, superheated-Melt, superheated-cooling, consolidation/sintering, cooling), (iii) Material State (Void, density, VOS), and (iv) Phase diagram and crystallization and composition contribution.

Finite difference Zeroth-Order Model **(ZOM)** algorithm was developed towards modelling of real-time calculation/prediction of thermal history in laser powder bed fusion (LPBF) process for both laser scanning (power and speed) and laser stationary (power) analyses [1]. **TMg** has been validated for Titanium [10] with respect to dynamic evolution of meltpool depth-width. It predicts Material State, as noted in Figure 8b-c. The tool can be used to define a dynamic process map that relates balling, humping, keyhole, unfused powder, no-melting, incomplete-melting, overheating, and stability to laser power and speed. Micro-scale thermal management model is shown in Figure 9. Stainless steel 316L Laser and Powder Bed Fusion (LPBF) in which the dynamic process map (P-V-T envelope) and the zones of stabilities and instabilities were validated for a single track of laser moving at different laser power and scan speed (range of P: 150-700 W and V: 300-750 mm/s). The predicted zones such as balling, humping, and stable regions) were compared with the literature data [11] and were in good agreement.

2.2. Phase Diagram Software Prediction

Due to the repeated thermal cycling that occurs with the processing

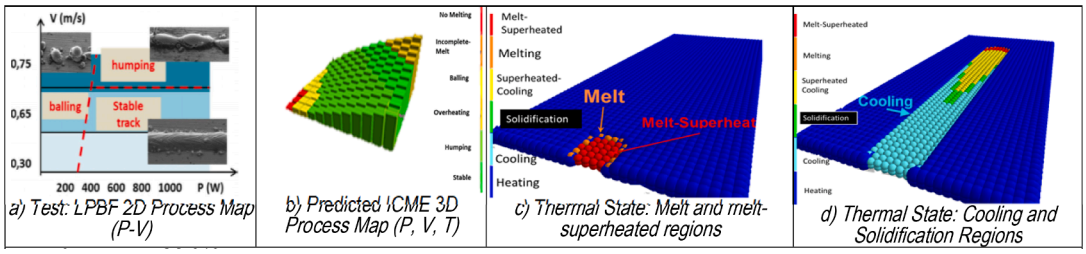

Figure 9. LPBF AM SS-316L Prediction/Validation different regions (humping, balling, stable)

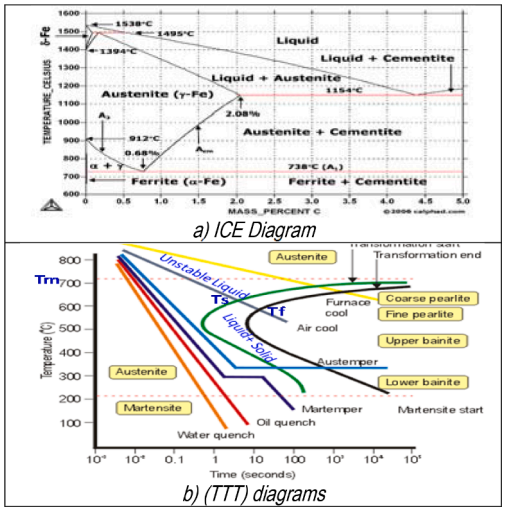

Figure 10. Metallurgy Diagrams for Steel [11]

of each subsequent layer, the microstructure of additively manufactured parts undergoes complex changes. It is important to understand the effect of time-temperature history for morphology of the metals which are used in the AM process. Studying the work of Kelly and Charles [12], a Ti-6Al-4V microstructural model has been developed which calculates the phase fractions, morphology, and alpha lath width given a measured or modelled thermal history.

ICME software predicts precipitates phase fractions vs. time. Equations and processes were used to calculate the final volume fraction of two different phases which resulted from thermal history. First, the time-temperature history is used as discretized data and Kinetic parameters used for phase percentage calculation. This parameter is totally dependent to the kind of material, in fact, this parameter is a physical parameter which needs to be considered based on material, heat treatment history and TTT diagram. The output of the calculation is estimation of phase percentages of the solid phases after AM process and cooling down. The solid phases are α and β at room temperature. The material type of α and β and phase percentage of α and β could then be used to estimate the mechanical properties of the manufactured material. Metallurgy diagrams for steel are three main diagrams that are extensively used in metallurgy, including iron-carbon equilibrium (**ICE**), continuous cooling transformation (**CCT**), and temperature time transformation (**TTT**) diagrams Figure 10 (**1**) *Phase-Iron-Carbon Equilibrium (ICE) Diagram*: ICE diagram means enough time allows heating and cooling, to any reactions, to fully complete, which includes information of the following: (**i**) what structure forms at what temperature and what carbon contents; (**ii**) what temperature difference composition melts; (**iii**) how much liquid and solid present at given temperature; **2**) *Temperature time Transformation (TTT) diagrams:* TTT determines the liquid to solid transformation where phase transformation occurs below the melting point (T_m). The thermal regions are: (**i**) stable liquid – doesn't intend to transform (T>Tm) region: superheat-cooling / fully-liquid, (**ii**) unstable liquid (undercooled liquid): intends to transform but has not yet started to transform (Tm<T<Ts) region: solidification, (**iii**) liquid + solid: some liquid has transformed, but transformation is not complete (between C curves – Ts< T< Tf) - region: solidification, and (**iv**) solid: when solidification is complete, all liquid has been transformed to solid. (T=Tf) Region: fully solidified. Crystallization begins at Ts and finishes at Tf including the unstable liquid and liquid + solid regions (as mentioned above steps ii, and iii). Also, growth rate is dominant at higher temperature which has a slower cooling rate resulting in coarse (large) grains. In contrast, the nucleation rate is dominant at lower temperature where there is a faster cooling rate, resulting in fine grains.

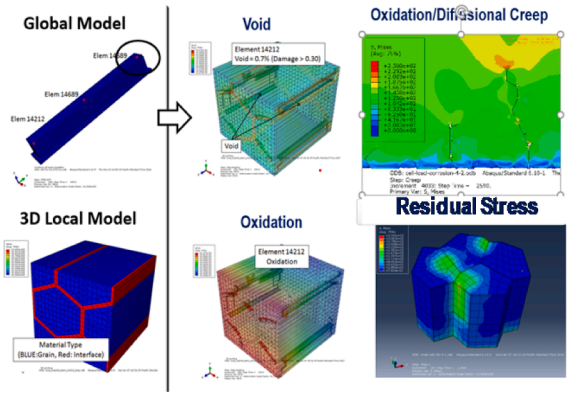

Figure 11. Global/Local Process Modeling, Grain Modeling and In-Service Crack Qualification.

2.3. ICME Simulation Elements

Are multi-scale models of thermal, mechanical, and material properties, as well as process models, and part qualifications with/without in-situ monitoring.

This toolset includes: **1**) a thermal management approach to rapidly calculate thermal profile, material state and process map; **2**) a global local FEM approach to calculate cracks, oxidation, surface roughness using diffusional creep approach; **3**) a fracture mechanics approach to determine fracture properties for 3D printed material system; **4**) a DOE (Design of Experiment) surrogate meta-modelling approach to optimize print parameters, minimize surface roughness, and obtain better surface finish. AlphaSTAR Corporation's (**ASC**) current ICME based 3D printing capability is used as baseline for the proposed metal AM process simulation. The current 3D printing computational tools include: material characterization, machine G-code data processing, mesh generation from G-code, STL file smoothing, as well as assessment of distortion, residual stress, deflection damage, and fracture evolution using coupled thermo-mechanical solution for both metal and polymer reinforced plastics. Figure 11 depict the current process flow strategy including material modelling and part qualification: (**i**) material characterization and qualification (**MCQ**) Software capability accounts for inclusions (particulate) to formulate stress strain curve in both longitudinal and transverse directions.

Micromechanic and fracture mechanic approaches have been developed (Figure 11) for the evaluation of the overall properties of heterogeneous materials and their dependence on the properties of constituents and the microstructure of materials [13]. They are mainly based on Eshelby's equivalent inclusion theory, a nano-mechanics based theory, proposed by Mori-Tanaka and Eshelby, used to demonstrate the capability of MCQ software to predict stress-strain curves with effect of inclusions. For fracture toughness determination (**FTD**) the extended Griffith theory is used to estimate the fracture toughness value of metallic alloys from simple uniaxial tensile tests. For fatigue crack growth (**FCG**), the fatigue crack growth rate curve (or da/dN vs. ΔK) can be generated by applying the fracture toughness value, K_C (obtained from the extended Griffith theory) for region, accelerated region, Paris region, and threshold regions; (**ii**) Part qualification uses durability and damage tolerance (**D&DT**) of a structure to assess the complex structures by performing a multi-scale progressive failure analysis to investigate what type of damage initiates, how it propagates, and how it leads to failure of the structure. Process modeling capability for powder metal includes the prediction of 3D printed global structure FEM, net shape, residual stress, local grain modelling, and diffusional creep using Voronoi tessellation mesh (2D), and effect of inclusion which predicts intergranular, and trans-granular cracks, residual stress and strain, and surface roughness, or 3D FE mesh, predicting surface roughness creep diffusion and inter-granular and trans-granular cracks which leads to

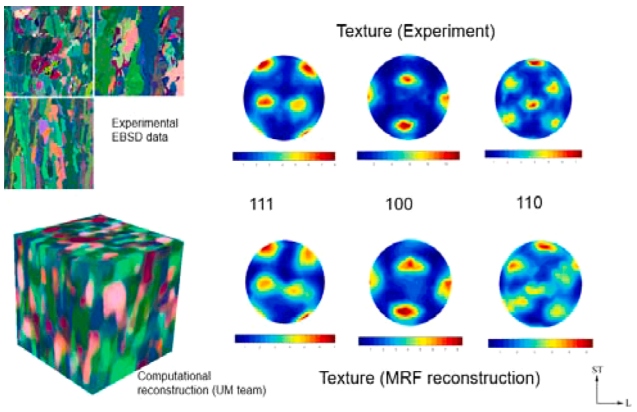

Figure 12. ESBD orthogonal set of images from the SLM Stainless steel

rupture. High values of triaxial tension can trigger void nucleation and growth leading to reduced creep ductility and creep-brittle behaviour. Using the elastic/plastic/creep modelling in the finite element analysis (**FEA)** allows the model to predict creep cracking based upon the multiaxial failure strain levels. AM process simulation developed by ASC includes both thermal and structural changes and is represented by coupled thermal-structural FEA. A transient coupled thermo-mechanical model is used to simulate the manufacturing behaviour when the fabricated part becomes distorted, and stress is built up during manufacturing because of the repeated heating and cooling. In-situ monitoring is used to measure surface roughness with big data processing.

2.4. EBSD software

Figure 12 demonstrates the output of an ICME visualization software that supports the 3D reconstruction of 2D EBSD data [14]. The technique can be used to perform rapid 3D statistical analysis of orientation correlation and grain boundary character using 2D orthogonal data sets. This data can subsequently be correlated to additive process parameters. The approach is unique and different from every other approach in literature, in that it reconstructs 3D microstructures directly from 2D sections, imaged on orthogonal planes, by exploiting the complete orientation space. The algorithm reconstructs 3D models through sampling voxel neighbourhoods to representative 2D micrographs, based upon a Markovian assumption. The sampling is followed by an optimization procedure, ensuring smoothness across the orthogonal sections of the synthesized voxels. The algorithm accurately represents orientations and orientation neighbour correlation, encompassing a variety of micrographs from EBSD and polarized light microscopy. The data can be used to perform rapid 3D statistical analysis of orientation correlation and grain boundary character using 2D orthogonal data sets, which can be subsequently correlated to additive process parameters. This presents a cost–effective methodology to study microstructures avoiding expensive 3D characterization techniques such as serial sectioning and high energy x-ray tomography. Figure 12 **(**top-left) shows the orthogonal set of images from the SLM Stainless steel sample. The 3D reconstruction from our software is shown (bottom-left); the reconstruction correctly captures the experimental texture as shown in the pole Figure 12 (right). The current focus is on the use of input by thermal model from **TMg** to develop large scale microstructures using ASC's LEGOMAT code and EBSD data. The LEGOMAT code places and extrapolates the 3D reconstructed microstructure on a CAD model based on thermal flow fields.

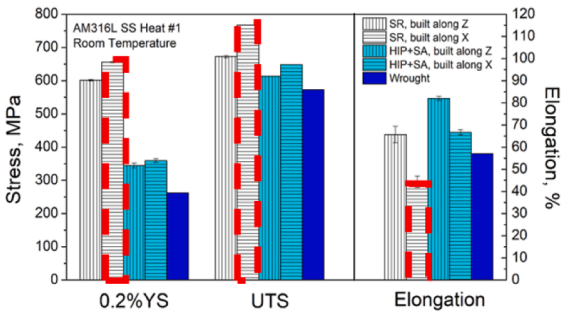

Figure 13. Stainless Steel stress factor

3. Experimental tests and measurements

3.1. Stainless steel of GE patented Grain Boundary Engineering

Was *demonstrated by post AM heat treatment CSL, and LAGB grain formation* [9] consisting of Post AM heat treatment of 316L-SS. Effect of heat treatment on microstructure was evaluated [6] using LPBF systems (EOS M270, EOS M280, Renishaw AM250). The laser process, heat treatment, and hot isostatic pressing (**HIP**) conditions were also systematically adjusted to understand the effects of process and heat treatment on the microstructure, porosity, and buildability.

Commercial SS-316L powder was used to fabricate AM 316L SS samples for this research. The powder was sieved using 325 mesh screens. To ensure the reasonable flowability, powder size below 15 μm was limited to < 3 wt.%. Table 2 shows the chemical compositions of the as-received powder and the AM made sample. The powder and the fabricated sample had a similar composition that met the ASTM A276 specification. The AM samples had a slight increase in oxygen and carbon, and a decrease in nitrogen, which was probably due to reactions (e.g., oxidation, nitrogen removal) during laser melting.

Heat treatment - Like laser process, *a variety of thermal heat treatment were also used* to control the microstructure and understand its effects on environmental cracking and irradiation properties. To give an example how heat treatment controls microstructure, Error! Reference source not found. shows a list of heat treatments used for a typical LPBF process with the parameters of 195 W laser power, 1.2 m/s laser scan speed, and 20 μm powder thickness.

Four heat treatment conditions were applied to AM 316L SS to assess the effect of microstructural variations: (**1**) no-treatment of as-built condition from LPBF; (**2**) stress relief at 650°C for 2 hours in argon, (**3**) HIP in argon for 4 hours at 1150°C and 1000 bar, followed by solution annealing (**SA**) at 1066 °C for 1 hour, and (**4**) heat treatment at 955°C for 4 hours in argon. Treatment 2 is called stress-relief because it releases some of the residual stress from the as-built component using a low-temperature treatment. Most AM 316L SS parts by AM vendors are supplied using either Treatment 1 or Treatment 2 if a heat treatment condition is not specified. Treatment 3 utilized HIP to densify the as-built part and recrystallize its microstructure. After the HIP process, a solution annealing at 1066 °C for 1 hour followed by a water quench was conducted to remove carbides that might form during the slow cooling following HIP. **Treatment 4** (955°C for 4 hours) was selected to produce a bimodal microstructure involving both recrystallized equiaxed grains (~30% recrystallized) and as-built characteristics, which was used in this study to understand the impact of the retained uncrystallized grains on SCC. In an AM part, full recrystallization is not always achieved due to the strain variations in the part. Solution-annealed AM materials generally possess some uncrystallized grains. Figure 13 compares yield, ultimate tensile and elongation for the four heat treatments and wrought.

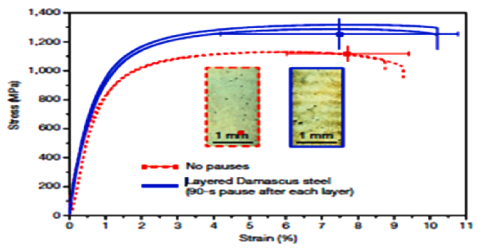

Figure 14. Process AM print of S-S Curve with Marging Steel, for Highstrength steel Damascus Steel (Fe19Ni5Ti)

3.2. Maraging Steel- and AM Damascus Steel higher strength

During the AM Process **[14]** the team used internal heat treatment (**IHT**) which consisted of multi-layer alternating of hard and soft layers and crystallization of Fe, Ni, and Ti (similar to Damascus steel). The process prints sandwich steel in which the 1st layer is hard and subsequent four layers soft only through the use of crystallization and machine parameter change. AM print of Damascus Steel (Fe19Ni5Ti), required IHT, and formation of martensite hardened by (Fe,Ni) 3Ti precipitates. Sample with the laser pause time (90 s) cools during the process and contains martensite hardened by (Fe,Ni) 3Ti precipitates. Figure 14 shows the tensile tests of two Fe19Ni5Ti (wt%) steel samples. One Damascus-like sample containing precipitation-hardened bands and a sample containing no precipitates. Two representative curves are shown for each condition together with the average value for maximum tensile strength and elongation at fracture (Tables 1 and 3).

4. Results, prediction and validation

4.1. TMg Process Thermal and Void Map

Figure 15 shows micro thermal model results: **a**) process map showing stable (green) and unstable regions (no-melting, over-heating, balling, incomplete heating) and **b**) void map. The print parameters considered here are unidirectional printing, 40 μm layer thickness, 100 μm laser focus diameter, hatch space 120 μm.

4.2. Thermal Management and Meltpool Engineering

The thermal history results of the two different steels are presented in Figure 16 **(**below**)** which shows: **a**) the results for stainless steel 316L (SS316L) and **b**) the results for Damascus steel. It should be explained that the thermal history of each case is affected by inclusions and precipitates of each steel. The precipitate of SS316L is SiO2 and the inclusions are nickel and chromium. For Damascus, however, the precipitate is martensite, and the inclusions are nickel and titanium. As is clear by the figure, the highest temperature of SS316L is higher than Damascus. It is considered because of the effect of precipitates and inclusions. In SS316L, SiO2 has an exothermic effect on the thermal process of this material causing the highest temperature to increase to 3102C. On the other hand, in Damascus steel, martensite has an endothermic effect which causes the highest temperature to become lower, calculated at 2000C. It should be noted that the results are presented from the central element through the thickness of the samples.

Figure 17 presents the temperature histogram of SS316L and Damascus steel. As is obvious for Damascus steel, 36% of the part is unfused. It is considered because of the endothermic effect of Martensite. It takes all the heat and does not allow the powders to become fused to each other; the surface of the powders becomes cooled and they cannot join to

Table 3
Heat treatment conditions and microstructural characteristics of AM SS-316L.

Condition	Thermal Treatment	Resulting Microstructure
Primary material in this study, Treatment 1 = As-built	None	Anisotropic, retained strain
Primary material in thus study, Treatment 2= Stress Relief	650°C for 2h in argon	Anisotropic, retained strain
Primary material in this study, Treatment 3 = HIP +SA	HIP for 4 h at 1150°C and 1000 bar in argon, followed by solution annealing at 1066°C for 1 hour	Fully-recrystallized like wrought 316L SS
Primary material in this study, Treatment 4 = Partial recrystallization	955°C for 4h in argon	Bimodal, partially-recrystallized (30% recrystallized)
High-porosity material = SA	1150°C for 2h in argon	Higher porosity, fully-recrystallized

Table 1
AM ICME Approach for GBE and New Alloy Design

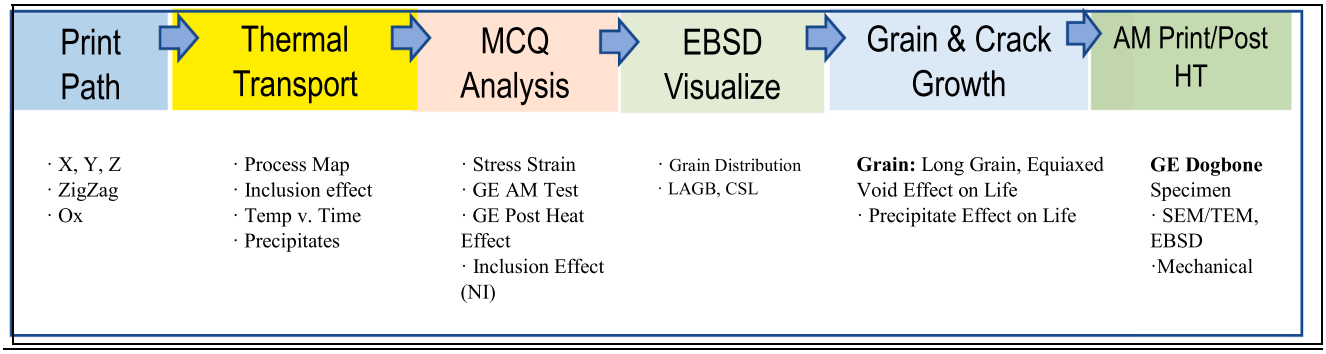

Table 2
Measured chemical compositions-AM SS-316L powder.

Material	Fe wt%	Cr wt%	Mn wt%	Si wt%	Ni wt%	Cu wt%	Mo wt%	V wt%	P wt%	Co wt%	W wt%	C wt%	S wt%	O wt%	N wt%
Powder	Bal.	16.7	1.02	0.074	10.7	0.19	2.29	0.05	0.02	0.13	0.04	221	62	326	1163
AM Part	Bal.	16.9	1.13	0.71	100.7	0.2	2.24	0.05	0.02	0.12	0.03	266	61	384	935

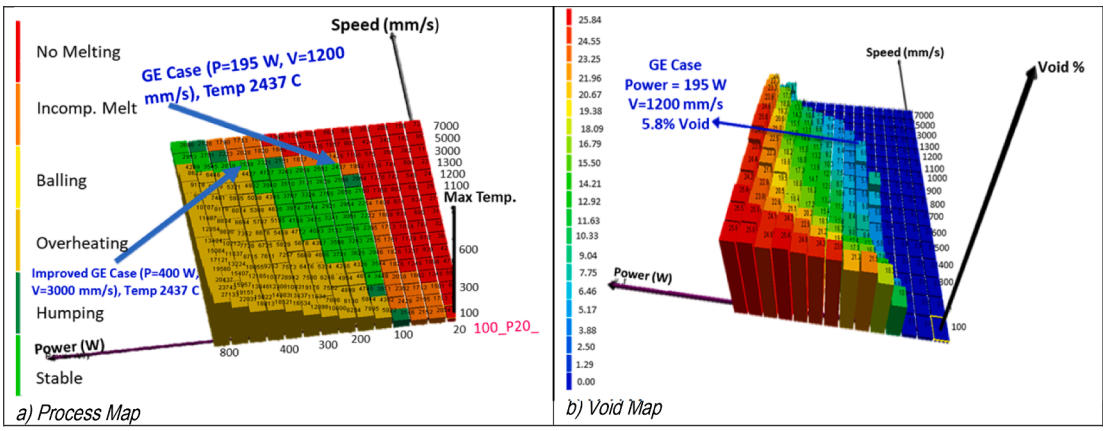

Figure 15. Process map and void map for LPBF printed Stainless Steel for the laser power range of 20 to 800 W and the laser speed range (100 mm/s to 7000mm/s)

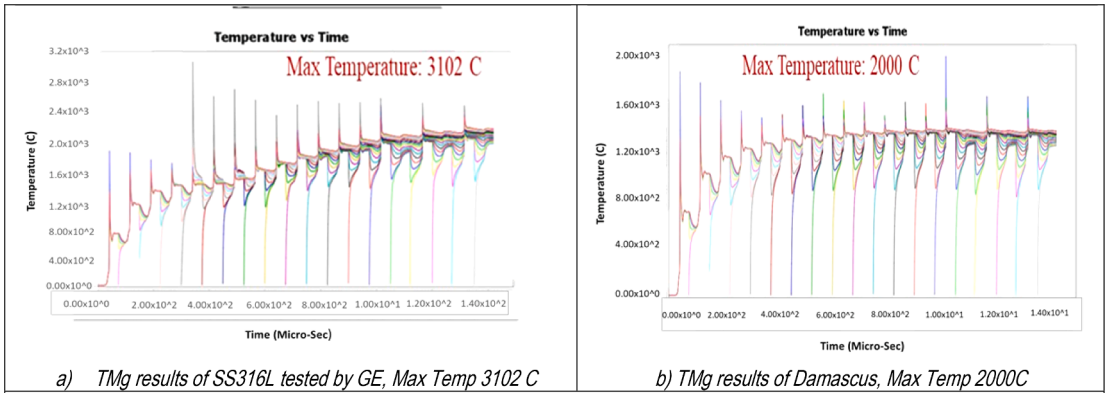

Figure 16. Thermal Profile of different Steels

each other.

For SS316L however, the percentage of the unfused materials is almost zero percent. SiO_2 in this material has exothermic effect which provides enough heat to melt the powders making them fused to each other. The maximum temperature happens for the chromium elements during the process. It is presented that 23% elements with the highest temperature in SS316L are chromium whereas Damascus steel's quantity is 3%. Figure 17 also compares structural voids and thermal conductivity between SS316L and Damascus steel. The void percentage in Damascus steel is higher because the unfused material is more in this material. The thermal conductivity of precipitates in SS316L is higher. Figure 18 illustrates the meltpool size of SS136L when there are no precipitates in the structure. As can be observed, the size of the meltpool is 190 × 50 × 140μm.

Thermal management analysis is also performed on a macro-level scale on a LPBF printed dog bone sample made of stainless steel. The model size is 25.4mm × 6.35mm × 0.8 mm (1" × 0.25" × 0.0315") which includes 1,197,560 elements and 20 layers. Figure 19**a** shows the modelled precipitation and inclusions complying with the usual composition of stainless steel. Figure 19 **b & c** show the void content & thermal conductivity prediction instantly at the end of the printing process, respectively. The LPBF printed dog bone thermal model predicts the temperature distribution in three sections: 1) Fused powder, 2) unfused powder, 3) and bottom plate (Figure 19**d**).

4.3. Material characterization and prediction of mechanical strength

Figure 20 presents the predicted stress strain curve of SS316L, after thermal treatment (stress relief at 650° for 2 hours), and Damascus steel. The results have been illustrated with the experimental test data. For SS316L, the predicted results are presented with the effect of CSL and HAGB. As it is clear, HAGB causes the strength to be very well matched with the experimental results. However, the yield strength is pretty much different from test data. On the other hand, the yield strength of the results by CSL is the same as the experiments, whereas CSL does not match ultimate tensile strength with the experimental results. The grain boundary angle degree selected here is 60°. Based on the results it can be concluded that the heat treatment results in the existence of both LAGB and CSL simultaneously in the microstructure. The predicted result of Damascus steel with just the effect of LAGB consideration is very well matched with the experimental test results which suggests that LAGB is present in the material microstructure. The considered boundary angle is 10°. It should be reminded that the boundary angle less than 15° is LAGB, otherwise it is HAGB. Based on Figure 20 **c and d**, the residual stress range in layers of Damascus goes up to 1500MPa which is higher than SS316L (250 MPa).

4.4. Phase Diagram and Precipitate Formation Prediction

The possible phases that can be produced during the manufacturing process has been predicted. Figure 21 shows an example of phase production with regards to phase and TTT diagrams of SS16L. By increasing the weight percentage of Ni, the percentage of austenite increases while ferrite decreases. It can be concluded that Ni supports austenite to become more stable till 1050°C. By cooling the material, the austenite transforms to precipitates such as silicon oxide and carbide.

4.5. Fracture Property Prediction of SS316 Steel Using LEFM

Figure 22**a**, illustrates the numerical predicted fracture energy as a

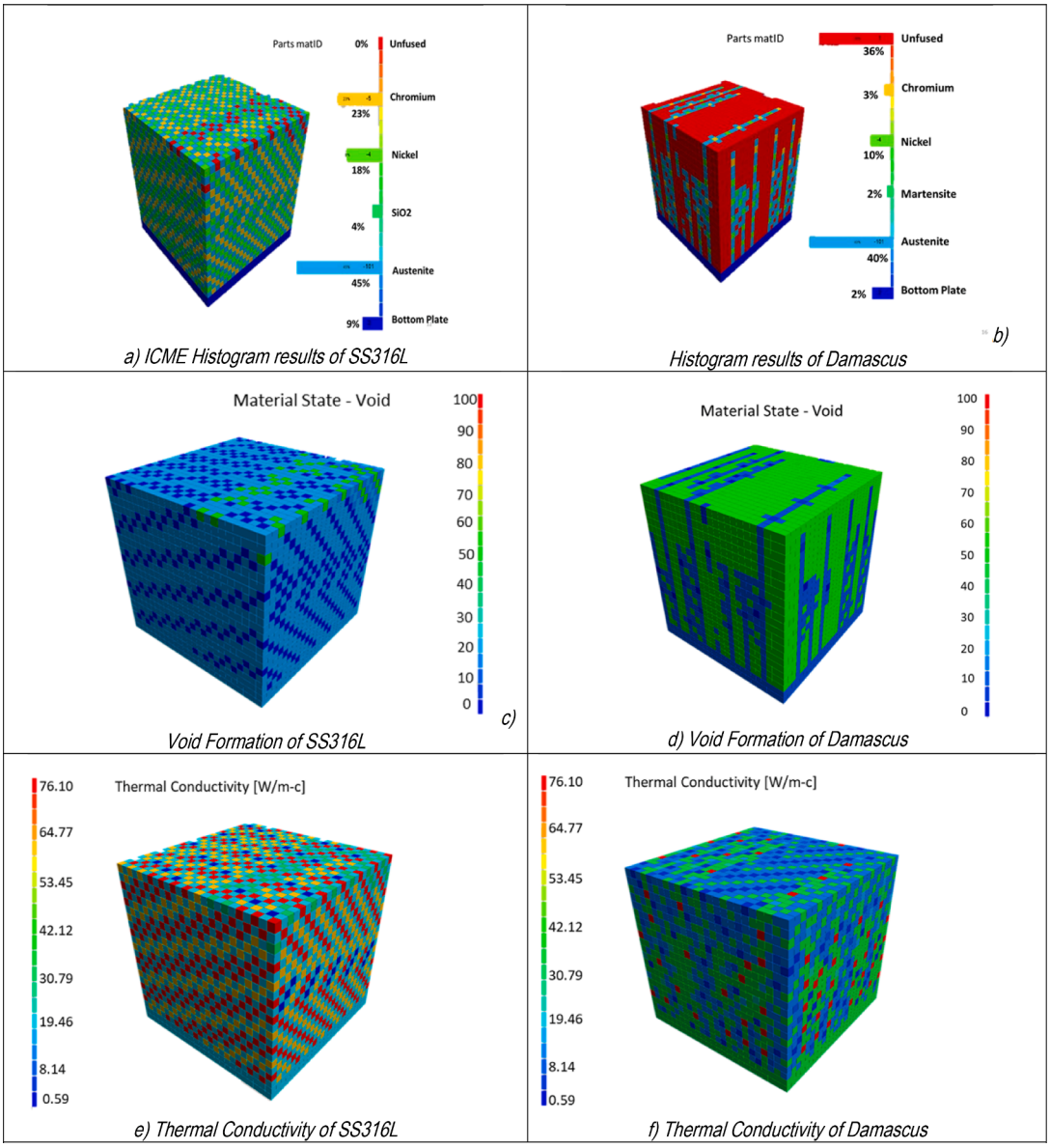

Figure 17. Steel composition, histogram (distribution) and effects on void, and thermal conductivity

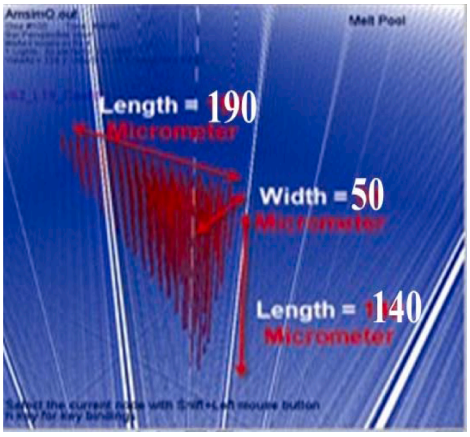

Figure 18. Meltpool size of SS316L without precipitate

function of specimen thickness for the heat-treated specimens. Figure 22**b** shows the experimental test results of Charpy impact test. In the experiments, the fracture energy for a specimen with the thickness of 10mm is 124J. The numerical predicted fracture energy shows the same number which is very well matched with the test data. Also, the fracture energy at plane strain situation is predicted to be 78J.

4.6. EBSD Prediction Measurement of HAGB and LAGB

EBSD reconstruction and grain boundary (**GB**) structure in 3D was analyzed for P= 400 w, S = 400 mm/s. Meltpool was evaluated (Figure 23**a**) by EBSD reconstruction and GB structure in 3D. Grain boundary misorientation angle (0 to 62 degrees) is shown in Figure 23**b**. Figure 23**c** shows the grain orientation's cross-sectional analysis.

4.7. Creep and Effect of Void and Precipitate on Grain Crack Growth

A local approach is pursued for predicting surface roughness and residual stresses. In this case, the local model is a finite element model which is augmented by the TR Crack code which effectively uses a

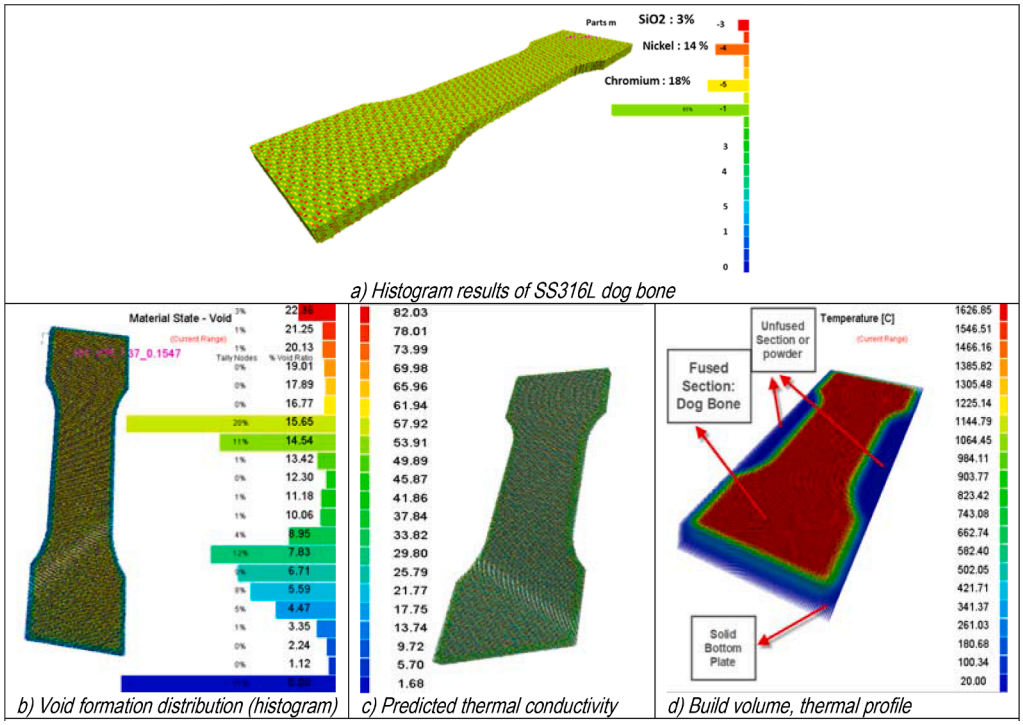

Figure 19. Dog bone model of SS316L and composition

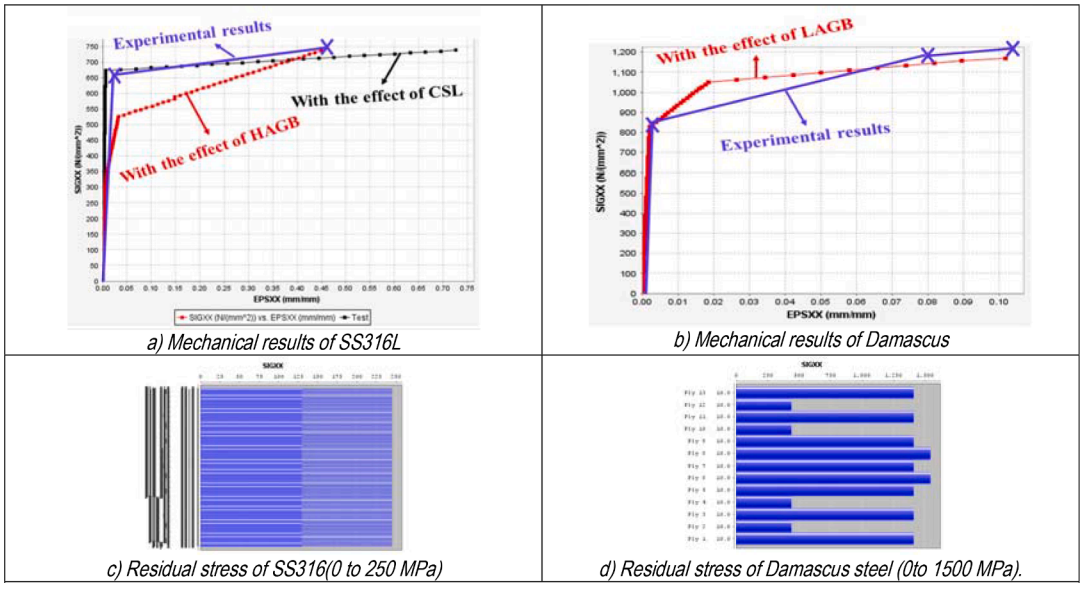

Figure 20. AM steel mechanical strength prediction compared with test.

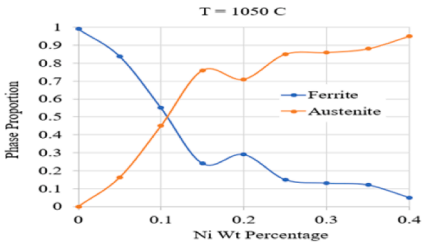

Figure 21. Phase diagram, precipitate formation prediction

multiaxial remaining creep ductility approach to predict the growth of voids and precipitates as microstructural entities in a grain/grain boundary microstructure. The input to the local model is the creep ductility at relevant temperatures derived from TMg simulation where the TMg modelling is used for localized area to calculate temperatures and material states when laser is passing. The local model used is a mesh structure consisting of grains (about 20-30 microns in size) and grain boundaries as shown in Figure 24**a.** The potential damage propagation region is established by the Voronoi tessellation method, which could produce grain and grain boundaries with voids and precipitates to simulate material microstructure. In the Voronoi cell finite element model, each cell represents a basic structural element of the

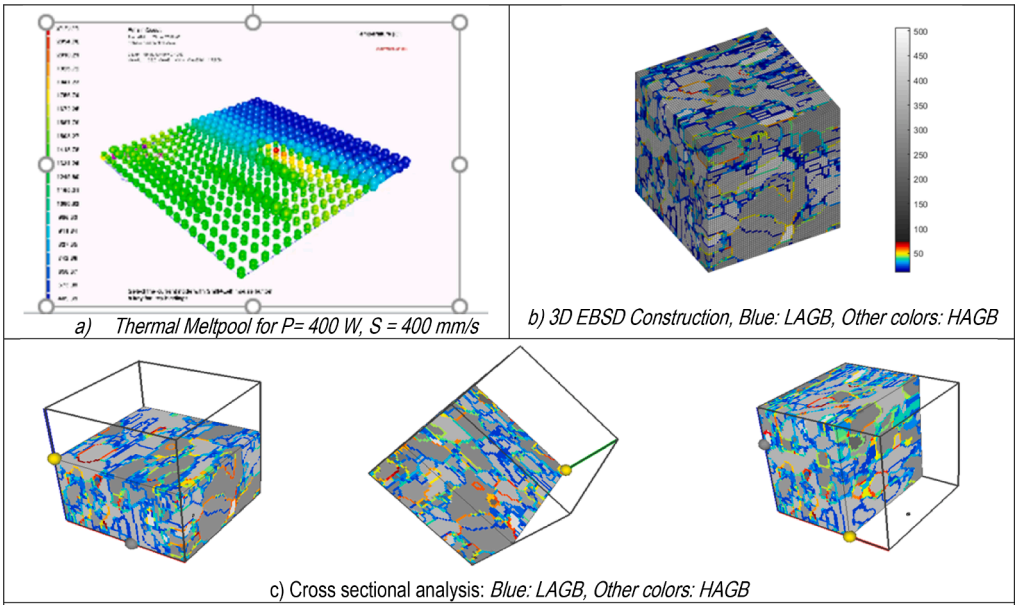

Figure 22. (a) Predicted fracture energy vs. thickness of the stress relief specimens along X direction; (b) Experimental results of Charpy test for different heat treatment conditions along X and Z directions for a sample with 10mm thickness.

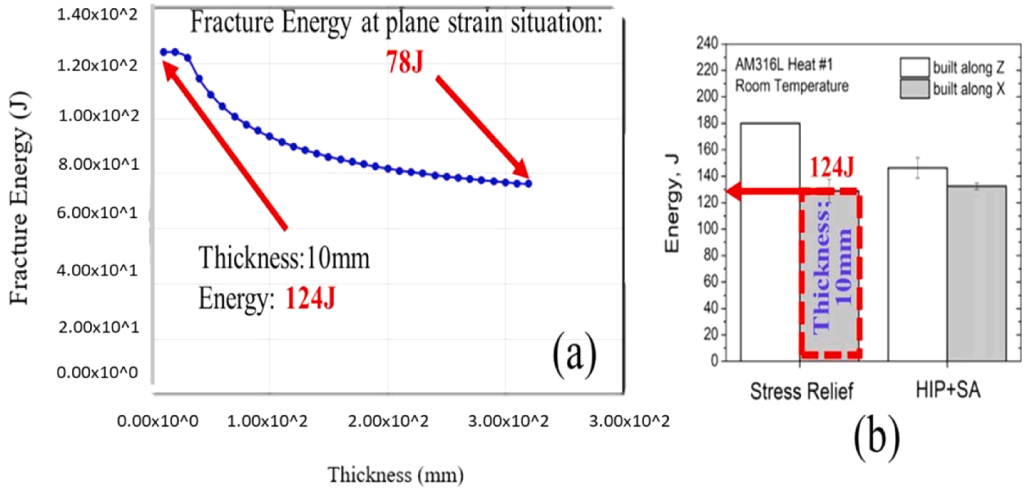

Figure 23. Grain Orientation Assignment-LAGB Vs HAGB

microstructure as well as a seed with its matrix neighbourhood. Seeds are generated randomly in MATLAB within a specified area. The boundary of each Voronoi cell is determined by its perpendicular bisector respect to its nearest neighbour seeds. The average radius of each Voronoi for the steel is expected to be 30-50 μm, representing the average grain size. The original Voronoi polygon boundary is offset with distance of 0.5 μm in both sides, leaving a fixed distance of 1 μm which is allocated as grain boundary thickness. Various densities of voids and precipitates are allocated randomly in different elements to simulate a real microstructure. Inter-granular and grain damages are calculated by the diffusional creep model, and the model degrades properties based on "remaining multi-axial creep ductility" to predict damage around, void, oxides, and surface roughness. Figure 24 **b** shows grains and grain boundaries in the model. The grain size is about 20 microns, while the grain boundary thickness is around 1 μm. Figure 24**c** shows the details of mesh used in the local model. The model has 65,504 nodes and 64,997 elements (element type ANSYS 181). The thickness is 40 μm for the model which is the same as layer thickness during the print. TMg simulation is ran based on fresh powder non-heat-treated cases with optimized parameters.

Figure 25 shows the temperature contours for the top layer resulted from TMg. These temperatures and same contours for the bottom layer are fed into the finite element local model. The material model for the local model is a linear elastic with different coefficients of thermal expansion for grains and grain boundaries. The properties are based on the fresh powder. The elastic modulus is degraded based on damages calculated by the TR Crack code using diffusional creep. In the local model, the boundary conditions are all 4 edges fixed in x and y and z to trigger the out of plane behaviour.

The finite element model is, as mentioned above, run for five temperature/loads, where the temperature also varies in the thickness of the shell. TR Crack code degrades the properties based on void and crack formations during the print where during cool-down, void formation, and the presence of residual stress and constrain play a significant part in the growth of voids and the consequent surface roughness. Figure 26**a** shows the surface roughness contours at the end of simulation (and the laser operation), where the maximum surface roughness is about 9 microns. Figure 26**b** illustrates the residual stresses due to

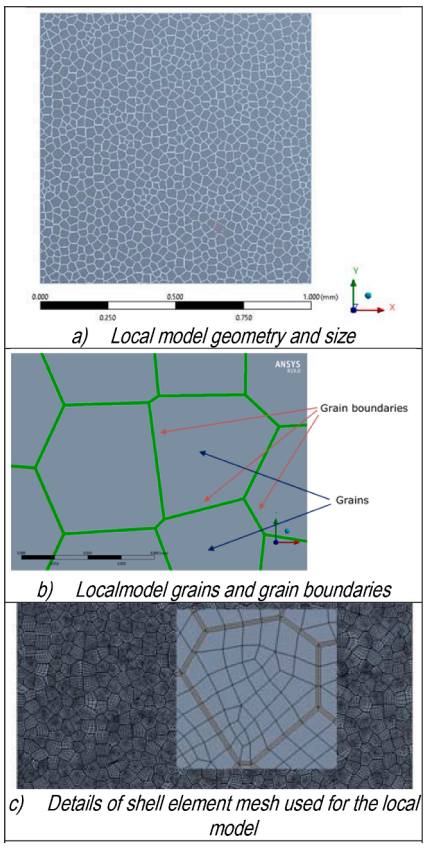

Figure 24. Geometry and details of the local model.

laser action at the end of simulation with maximum residual stress of 4700 MPa. Figure 26**c** and Figure 26**d** also demonstrate the prediction of local model for damages in grains and grain boundaries as well as creep strains when the laser action is complete.

4.8. *Life Predictions, Crack Growth and Effect of Void and Precipitate*

To predict the effects of voids and precipitates and their effect on the performance of the material under creep load, a model with mixed irregular elongated grains is used. This type of mesh with complex grain structures allows the simulation of grain/grain boundaries and void and precipitate distributions to predict component response to failure more realistically. This is achieved by quantitatively characterizing the grain and grain boundary regularity and density in the microstructure. Figure 27 schematically compares the regular grains with the new mixed irregular elongated grains used in this study. Figure 27**c** demonstrates the microstructure meshing structure at the crack region of a compact tension (**CT**) sample. This approach effectively allows TR Crack to simulate creep crack growth for materials with and without void. As an example, simulations on steel shown in Figure 28 suggest that that presence of random voids with different density distribution could drastically reduce the life of material. This is evident in Figure 28**c** where 1% void causes almost 30% decrease in creep life. On the other hand, precipitates which are effective high strength material dispersed in a microstructure can be shown to increase the creep life and improve the performance of material. Figure 28**a & b** compares crack growth for the material with and without precipitates. Simulations suggests that a small amount of precipitate will lead to a 22% increase in creep life which is shown in Figure 29. This approach will allow the development of more complex microstructural systems which are relevant to AM manufacturing and allow rapid sensitivity analysis of simulations of materials which contain different ovalities or possible lamellar grain structures containing random densities of voids and precipitates.

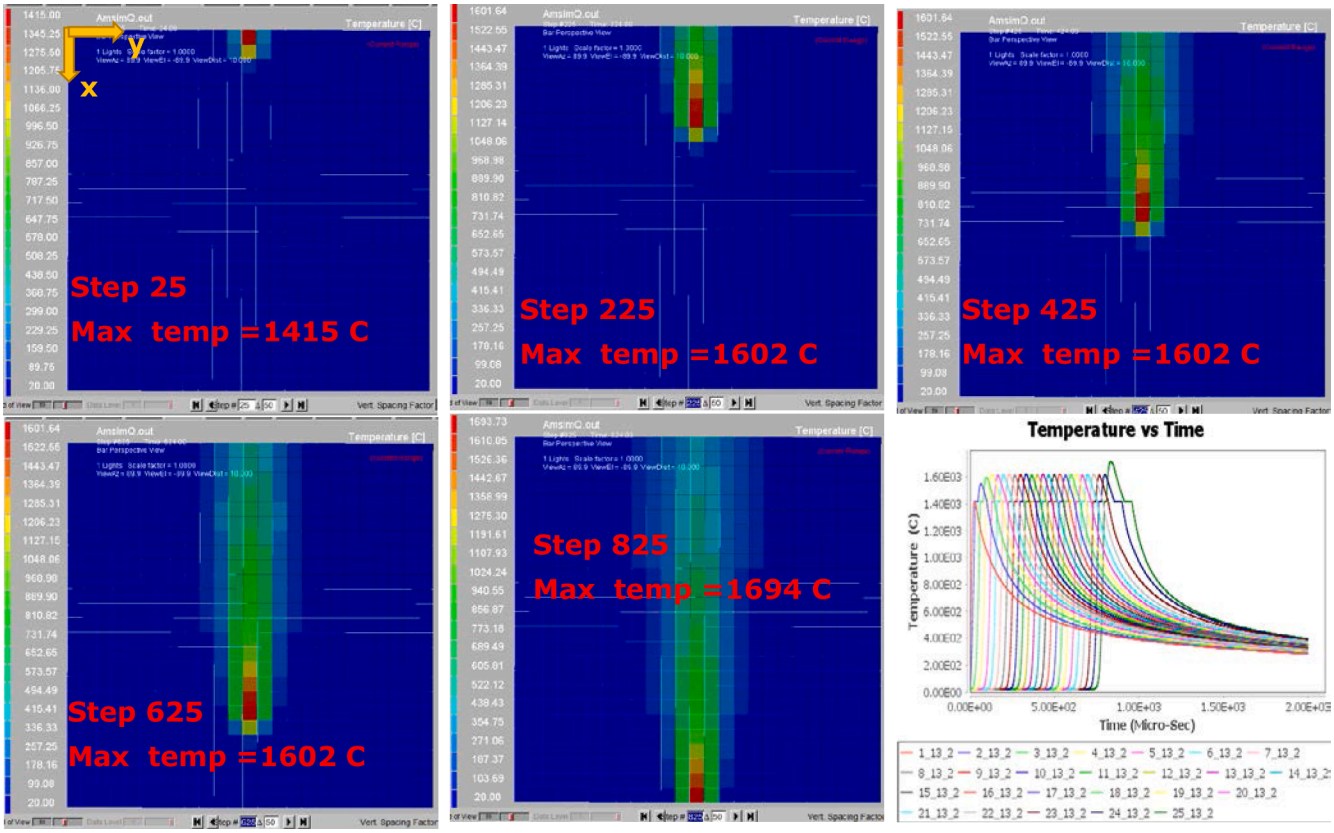

Figure 25. Temperature variations of top surface due to laser operation calculated by TMg for the local model.

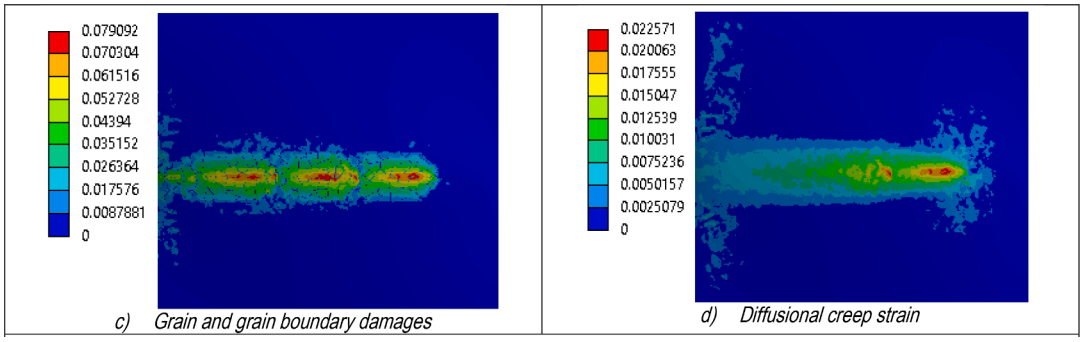

Figure 26. Predictions of local model for surface roughness, residual stresses, damages, and diffusional creep.

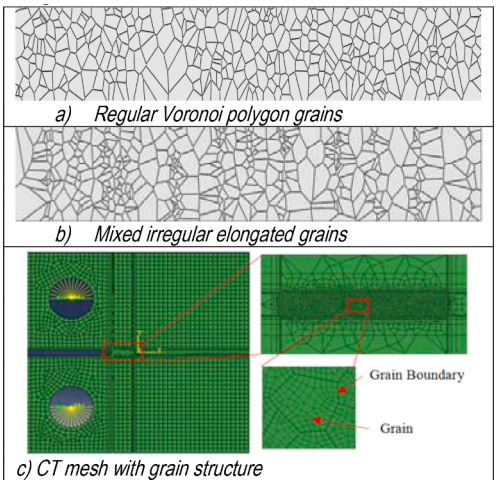

Figure 27. Regular vs mixed irregular grains.

4.9. Fabrication and Post Heat Treatment Print of Dog bone Specimen and Prediction Comparison

AM Print of SS-Steel 316 dog-bone specimen was performed, using EOS M290 LPBF machine. Figure 30**a** shows 25 specimens printed (P=195 W, LS=1200mm/s, Hatch Space =0.1 mm, Energy = 40.63 J/mm^3. Figure 30**b** shows the SEM image of no heat treatment. The post AM heat treatment conditions are: **a**) twelve (12) heat treated specimens at (650°C, 2 hrs): **b**) four (4) air cooled specimens, and **c**) four (4) water quenched specimens). A mechanical properties test was performed showing improved strength-stain curve that verifies the GE patent.

5. Conclusion

An ICME toolset was developed to predict the microstructure of AM parts; assess the sensitivity of the build in terms of process parameters, build plan, and mechanical properties; and optimize the build process to minimize defects, achieve desired microstructure and improve part quality. The goal of the overall effort was grain design and grain boundary engineering to achieve desired outcomes. Modules developed to support this effort included: (i) thermal transport and void prediction;

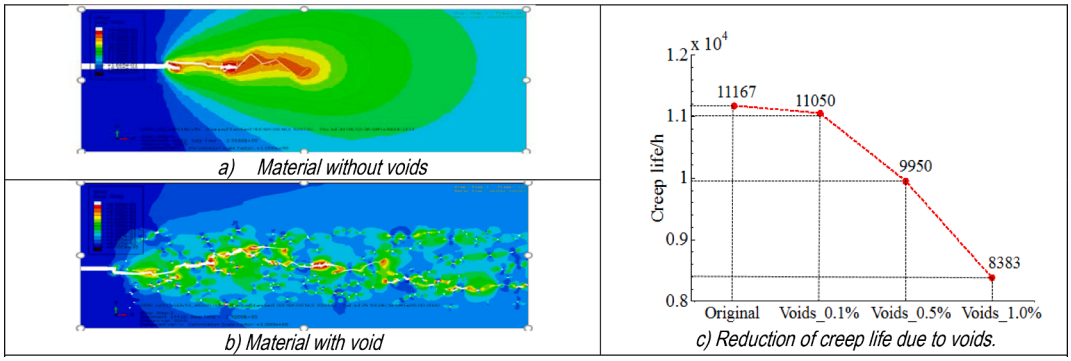

Figure 28. Crack growth for material with and without voids for CT at 550°C.

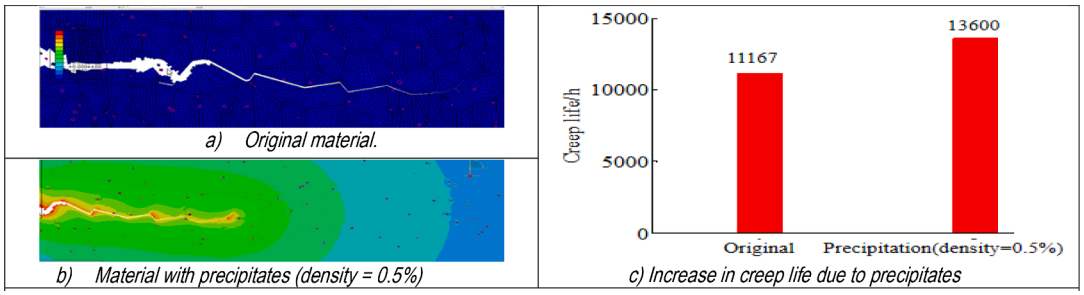

Figure 29. Crack growth for material with and without precipitates for CT.

Figure 30. GE AM print of SS-316 steel specimen, tensile test, and NDE

(ii) material characterization and prediction of mechanical and fracture properties; (iii) creep diffusion and crack growth for prediction of surface roughness, (iv) phase diagram and microstructural kinetics, and (v) EBSD texture reconstruction and visualization that reflected microstructural changes. Utilizing an LPBF platform, dog bone specimens were fabricated to validate predictions and validations were used to drive part microstructure in the form of preferred grain boundaries.

The initial application of the tool sought to improve the mechanical properties of an AM dog bone subject to post build heat treatment, Utilizing build parameters provided by the patent holder, the team accurately predicted the quality of the build outcome and devised virtual heat treatment strategies. The utilized heat treat resulted in improved strain for the finished. NDE and DE examination of printed specimens also corroborated the increased presence of LAGB. A second virtual/physical build sought to improve mechanical properties without resorting to post build heat treatment. Here, the tool was called upon to predict the thermal history, material state, and process to identify stable and unstable regions in the build and optimize those values to address a single criteria or multi-criteria concern. The methodology was used to identify process parameters that corresponded to a desired microstructure and a build plan that leveraged latent cooling to effect material crystallization and precipitation. The on again off again approach provided a framework laser supported hardening of the steel. Results were promising. Fabricated dog bones exhibited measurable increases in both strength and strain and EBSD visualization confirmed that the presence of low angel and coincident site lattice grain boundaries. Further tests were needed to fully validate the process. In the final component of the program, the team sought to improve microstructure by exploiting the

process of precipitation and the effect of nano-inclusions on microstructure during the AM process. The approach corresponded to the design of a new alloy with improved mechanical and fracture properties of polycrystalline steels. Results showed that in SS316L, SiO_2 has an exothermic effect which provided enough heat to melt and fuse powders. Once again, changes to mechanical properties and microstructure were promising and deserving of further research strength. The microthermal and mechanical behaviour of SS316L and Damascus steels were annualized in this research. However, in Damascus steel, with maraging steel powder distribution the endothermic effect of Martensite takes all the heat and does not allow the powders to become fused to each other. The experimental tests observation showed that with the heat treatment of the specimens, the fracture toughness of the materials decreases, and the cooling condition has no effect on the resulted mechanical properties. Further investigation is warranted. Future efforts will conduct additional studies of optimization of microstructure of polycrystalline materials and the corresponding changes to finished AM parts Here, density, finish, net shape and in-service loading will be a focus. Additional focus will be given to: **a**) inclusion effect, **b**) cooling (i.e., nitrogen, helium, argon) on precipitation, **c**) print path orientation on LAGB/HAGB grain microstructure, and **d**) machine parameters to maximize mechanical strength, fracture toughness, and life cycle fatigue during AM and post heat treatment.

Declaration of Competing Interest

The authors declare that they have no known competing financial interests or personal relationships that could have appeared to influence the work reported in this paper.

References

[1] M.F. Ashby, Kenneth Edwin Easterling, The transformation hardening of steel surfaces by laser beams—I. Hypo-eutectoid steels, Acta Metall. 32 (11) (1984) 1935–1948.

[2] Z. Ruslan, Valiev a,1, Terence G. Langdon “Principles of equal-channel angular pressing as a processing tool for grain refinement, Prog. Mater Sci. 51 (2006) 881–981.

[3] Frank Abdi, Mohit Garg, Characterization of Nanocomposites Technology and Industrial Applications, Pan Stanford Publishing Pte. Ltd, February 2017. ISBN 978-1-315-36489-6 (eBook), Book published by.

[4] GE-Patent: Lou, Xiaoyuan, Dolley, Evan Jarrett, Morra, Martin Matthew, "Grain Boundary Engineering For Additive Manufacturing", 2018. http://www.freepatentsonline.com/y2018/0085830.html.

[5] Jennifer Nguyen Wolk, Microstructural Evolution In Friction Stir Welding Of Ti 5111”. Doctor of Philosophy, Thesis in Dissertation submitted to the Faculty of the Graduate School of the University of Maryland, College Park, in partial fulfillment of the requirements for the degree of Doctor of Philosophy, 2010.

[6] Behzad Sadeghi, Pasquale Cavaliere, Martin Nosko, Veronika TremboŠovÁ, Štefan Nagy, Hot deformation behaviour of bimodal sized Al2O3/Al nanocomposites fabricated by spark plasma sintering, J. Microsc. 281 (1) (2021) 28–45.

[7] Iman Javaheri, Veera Sundararaghavan, Polycrystalline Microstructure Reconstruction Using Markov Random Fields and Histogram Matching, Comput. Aided Des. (2019), 102806.

[8] L. Liza Chan, Synthetic three-dimensional voxel-based microstructures that contain annealing twins (PhD thesis), Carnegie Mellon University Pittsburgh, PA, 2010.

[9] GE-Report:Raul B. Rebak, Xiaoyuan Lou, Gary Was, Francis T. Bolger, Fredrick A List III.,”Environmental Cracking and Irradiation Resistant Stainless steel by Additive Manufacturing”, GE Global Research Structural Materials Technologies, Award #: DE-NE0008428. Final report. 30 March 2018.

[10] Frank Abdi, Clement Tam, Stephen Anderson, Nima Moazami, Kamran Nikbin, Cody Godines, Gyaneswar Tandon, Vasyl Harik*and* Rashid Miraj, "Sensory Real-Time In-Situ Monitoring Toolset for Additive Manufactured Parts, SAMPE J. (Nov-Dec, 2019).

[11] Valérie Gunenthiram, Patrice Peyre, Matthieu Schneider, Morgan Dal, Frédéric Coste, Rémy Fabbro, Analysis of laser–meltpool–powder bed interaction during the selective laser melting of a stainless steel, J. Laser Appl. 29 (2) (2017), 022303.

[12] S.M. Kelly, Thermal and Microstructure Modeling of Metal Deposition Processes with Application to Ti-6Al-4V, Virginia Polytechnic Institute and State University, Blacksburg, VA, 2004.

[13] Frank Abdi, Yibin Xue, Mohit Garg, Bob Farahmand, Jerry Housner, Kamran Nikbin, An Analysis Approach toward FAA Certification for Damage Tolerance of Aircraft Components, Royal Society Journal (Jan 2014).

[14] P. Kürnsteiner, M.B. Wilms, A. Weisheit, B. Gault, E.A. Jägle, D. Raabe, High-strength Damascus steel by additive manufacturing, Nature 582 (7813) (2020) 515.